Applied Thermal Engineering 259 (2025) 124804

Contents lists available at ScienceDirect

Applied Thermal Engineering

journal homepage: www.elsevier.com/locate/apthermeng

Research Paper

# Experimental and numerical investigation on a hybrid high-temperature downhole thermal management system integrating liquid cooling and phase change material

Jiale Peng [a], Jiacheng Li [a], Siqi Zhang [a], Guanying Xing [a], Jinlong Ma [a], Bofeng Shang [b,*], Xiaobing Luo [a,*]

[a] School of Energy and Power Engineering, Huazhong University of Science and Technology, Wuhan, China
[b] Key Laboratory of Materials Physics, Ministry of Education, School of Physics, Zhengzhou University, Zhengzhou, China

ARTICLE INFO

*Keywords:*
Downhole thermal management system
Liquid cooling
Phase change material
Temperature difference
Workable time

ABSTRACT

The downhole electronics must operate in an extremely thermal environment for several hours. Previous researches have proved that passive thermal management systems (PTMSs) are able to protect downhole electronics over extended durations. However, conventional PTMSs commonly suffer from a significant thermal resistance between the electronics and phase change materials (PCM), which restricting the efficient heat transfer to the PCM and consequently reducing the effective operating time. In this study, a hybrid thermal management system (HTMS) integrating liquid cooling and phase change thermal energy storage technique was proposed to enhance the internal heat transfer performance of downhole electronics and extend the operation duration. An active heat transfer channel was established between the electronics and PCM through liquid cooling system, and thus the generated heat was efficiently transferred and stored in PCM. The thermal performance of the proposed HTMS was investigated both experimentally and numerically. The accuracy of the numerical model was validated through experimental results, with a deviation lower than 6 %. The experimental results show that the temperature difference between the heat source and the heat storage module (HSM) was reduced by up to 51.9 °C, and the workable time was increased by up to 166 mins compared to the system without liquid cooling. The proposed HTMS exhibits superior heat transfer performance, which contributes to achieving a longer effective operation duration and holds extensive and profound application prospects in the field of thermal management for downhole electronic devices.

## 1. Introduction

Oil and gas resources are critical as fossil energy sources in many areas around the world [1,2]. As shallow oil and gas resources are exhausted, deep exploration becomes increasingly important [3,4]. Logging tools, as specialized equipment for petroleum resource, are lowered downhole to obtain rock formation information to determine the distribution of oil and gas underground. The ambient temperature might exceed 200 °C when logging tools operate in a well with a depth of more than 5 km [5,6]. The downhole electronics in logging tools cannot withstand such high temperatures for long time [7,8]. Without thermal protection, downhole electronics may quickly exceed their temperature tolerance and fail [9–11]. Therefore, effective thermal management measures are highly important to protect the normal operation of downhole electronics.

There are several studies focusing on thermal management systems (TMSs) for downhole electronics, including active thermal management systems (ATMSs) and passive thermal management systems (PTMSs) [12,13]. ATMSs can be divided into vapor compression refrigeration, split-Stirling refrigeration, thermoelectric refrigeration, and thermoacoustic refrigeration [14–22]. ATMSs transfer the heat generated by the electronics to the high temperature environment through the additional power input, which is beneficial for long-time operation, but the reliability in high temperature downhole environments is still doubtful. Up to now, no successful downhole application of these ATMSs has been reported.

In contrast, PTMSs have been widely used in downhole electronics due to their excellent reliability without additional energy input, thus the system architecture is relatively simple. In addition, the PTMSs

* Corresponding authors.
*E-mail addresses:* shangbofeng@zzu.edu.cn (B. Shang), luoxb@hust.edu.cn (X. Luo).

https://doi.org/10.1016/j.applthermaleng.2024.124804
Received 16 August 2024; Received in revised form 13 October 2024; Accepted 3 November 2024
Available online 5 November 2024

**Nomenclature**

| | |
|---|---|
| $Re$ | Reynolds number |
| $\mu$ | Dynamic viscosity of coolant |
| $d$ | Pipe diameter |
| $u(T)$ | Uncertainty in temperature measurement |
| m | Uncertainty in thermocouple temperature measurement |
| n | Uncertainty in temperature measurement by data acquisition instrument |
| $\rho$ | Density |
| $c$ | Specific heat capacity |
| $\lambda$ | Thermal conductivity |
| $T$ | Temperature |
| $t$ | Time |
| $u$ | Velocity of coolant |
| $P$ | Pressure of coolant |
| $q$ | Heating power per unit volume |
| $q_h$ | Heating power per unit volume of heat sources |
| $q_m$ | Heating power per unit volume of micropump |
| $L_m$ | Latent heat of PCM |
| $c_{eff}$ | Equivalent heat capacity of PCM |
| $\theta$ | Volume fraction of liquid PCM |
| $V$ | Volume |
| $h_L$ | Average convective heat transfer coefficient |
| $r_h$ | Radius of the wellbore wall |
| $r_t$ | Radius of the logging tool |
| $L$ | Length of the logging tool |
| $a$ | Thermal diffusion coefficient |
| $\varphi$ | Reynold stress |
| $q_{out}$ | Heat density from high-temperature environment |

*Subscripts*

| | |
|---|---|
| $s$ | Solid materials |
| $l$ | Coolant |
| $in$ | Inlet |
| $out$ | Outlet |
| $PCM$ | PCM |
| $PCM\text{-}s$ | Solid PCM |
| $PCM\text{-}l$ | Liquid PCM |
| $onset$ | Start of phase change |
| $end$ | End of phase change |
| $mud$ | Mud |
| $bottle$ | The outer wall of vacuum bottle |
| $t$ | the logging tool |
| $h$ | the wellbore wall |

*Abbreviations*

| | |
|---|---|
| TMS | Thermal management system |
| ATMS | Active thermal management system |
| PTMS | Passive thermal management system |
| HSM | Heat storage module |
| PCM | Phase change material |
| HTMS | Hybrid thermal management system |
| TIM | Thermal interface material |
| LMPA | Low melting point alloy |

demonstrated exceptional temperature control performance during the phase change transition process [23,24]. PTMSs are composed of thermal insulation components, heat storage material and specific structure for heat transfer enhancement. Firstly, the heat transfer from the high temperature environment to the inside of the logging tools is hindered by the vacuum bottle with a vacuum layer and the thermal insulators made of low thermal conductivity material [25–27]; secondly, the self-generated heat of the downhole electronics and the heat intrusion from the external heat transfer are stored by the heat storage module (HSM) [28–30]; thirdly, the heat-transfer channel between the downhole electronics and the HSM is constructed to strengthen the heat transfer [31–33]. The above techniques enable downhole electronics to operate normally for a period. However, due to the limited heat transfer capacity of conduction, once the heating power of downhole electronics is excessively high or the heat transfer distance is long, the thermal resistance of heat transfer between the heat source and the HSM is relatively large. Consequently, the downhole electronics would reach the tolerance temperature immediately while not fully utilizing heat storage capacity of HSM, thereby reducing their operational time.

Currently, liquid cooling systems have been relatively mature and widely used in various industries due to the exceptional long-distance heat transfer capacities and heat dissipation capacity [34–39]. Recently, researchers have introduced liquid cooling systems into TMS for downhole electronics. Jakaboski [40] proposed an innovative thermal management system that combines the liquid cooling and phase change material (PCM). The experimental results show that by using water as a coolant, the instrument can operate normally for 28 h with a total heating power of 18 W, a length of 2362 mm and a diameter of 84.8 mm. Ma et al. [41] conducted an experimental study on active thermal protection for downhole devices used in deep downhole environment exploration. The results show that using water as cooling medium, the flow rate of 200 ml/min can extend the working time of the device to 5 h. Peng et al. [42] proposed a hybrid thermal management system (HTMS) for downhole electronics is proposed to prolong the workable time, the results show that the hybrid thermal management system increases the operating time of the electronics from 230 min to 450 min. The above studies have provided qualified resolution for the thermal management under specific circumstances. However, it is imperative to conduct a comprehensive investigation into the percentage of heat transfer and heat storage within the system. Additionally, the

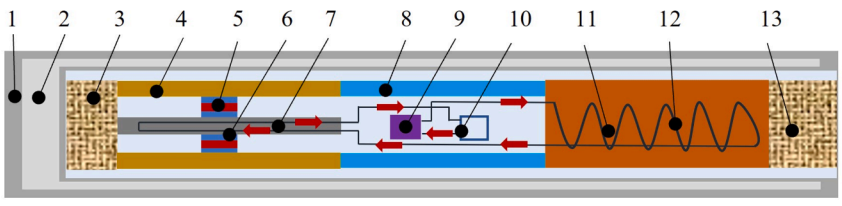


**1. Vacuum bottle 2. Vacuum layer 3. Insulator 1 4. Covers**
**5. Heat sources 6. TIMs 7. Cold plate 8. Adapter 9. Micropump**
**10. Liquid compensator 11. HSM 12. Spiral pipes in HSM 13. Insulator 2**

**Fig. 1.** The schematic structure of a high-temperature downhole TMS integrating liquid cooling and PCM.

**Table 1**
Materials and thermal properties of the logging tool [26].

| Name | Material | Thermal conductivity ($W \cdot m^{-1} \cdot K^{-1}$) | Density ($kg \cdot m^{-3}$) | Heat capacity ($J \cdot kg^{-1} \cdot K^{-1}$) |
|---|---|---|---|---|
| Vacuum bottle | Inconel 718 | 14.7 | 8240 | 436 |
| Vacuum layer | Composite | 0.0002 | 100 | 1200 |
| Adapter and cover | Aluminum alloy 6061 | 167 | 2710 | 896 |
| Cold plate | Copper | 400 | 8700 | 385 |
| Heat sources | Ceramic | 30 | 3960 | 850 |
| Heat-conductive silicone pads | Silica gel | 1 | 1810 | 923 |
| PCM | Low melting point alloy (LMPA) | 18.42 | 9660 | 132(s)/138(l) |
| PCM container and pipe | 304 | 16.3 | 7930 | 500 |
| Insulator shell | PEEK | 0.25 | 2200 | 1000 |
| Insulator core | Aluminum silicate wool | 0.035 | 400 | 794.2 |
| Coolant | Thermal oil | 0.143 | 965 | 1400 |

impact of the heat generated by the micropump in the liquid cooling system on TMS remains unclear. Therefore, it is essential to consider the thermal effect of the pump itself and propose an appropriate numerical model for investigating internal heat transfer within the system. Furthermore, experimental tests are necessary to verify the reliability of the thermal management system when subjected to varying heating power.

In this study, a high-temperature downhole HTMS integrating liquid cooling and PCM was proposed. In this system, the micropump was introduced to facilitate the efficient transfer of heat generated by the electronics to PCM. A prototype was fabricated and an experimental rig was built to conduct experimental test under different heating powers. To systematically investigate the thermal performance of the proposed system, a numerical model considering the inherent heat generation of the micropump was developed to simulate the transient flow and heat transfer. The temperature distribution, phase change behaviour, heat flux, and the percentage of heat generation and absorption were analysed.

## 2. Experimental section

### 2.1. Thermal management system

Fig. 1 shows the schematic structure of a high-temperature downhole TMS integrating liquid cooling and PCM. The proposed system comprises a vacuum bottle, two thermal insulators, heat sources, thermal interface materials (TIMs), covers, a cold plate, an adapter, a HSM, a micropump, a liquid compensator, coolant, spiral pipes in HSM, and other pipes. All physical parameters are detailed in Table 1. To reduce the effects of the high-temperature environment environments, the vacuum bottle with a vacuum layer and the thermal insulators provide radial and axial thermal insulation, respectively. The total length of the vacuum bottle is 908 mm, with an internal mounting skeleton length of 848 mm. The outer and inner diameters of the vacuum bottle are 90 mm and 73 mm, respectively. The vacuum layer, with a thickness of 3 mm, is situated between these outer and inner diameters. Both thermal insulators have a diameter of 72 mm, with thermal insulator 1 measuring 28 mm in length and thermal insulator 2 measuring 150 mm in length.

Although the vacuum bottle and thermal insulators effectively shield the system from the high-temperature environment, the electronics (consider as heat sources) generate additional heat during operation. The excess heat needs to be stored by the HSM. Fig. 2 illustrates the structure of the HSM, which consists of three sections. The first section is the container of the HSM including two mounting tabs. The first tab mates with the thermal insulators and features a potting seal for potting the PCM. The other tab, designed for mounting the adapter, has a pagoda-shaped end for coolant sealing. The second section contains the spiral pipes in the HSM. The final section is the encapsulated PCM within the container. The length of the HSM is 320 mm with the diameter of 72 mm.

A high heat storage rate of the PCM promotes homogenization of the system and extends its operation time. The heat storage density of the PCM, including both the latent heat storage and sensible heat storage, is crucial for the system's performance [43,44]. Therefore, the PCM for the downhole TMS must have a high heat storage rate and heat storage density. In addition, the PCM need to have a small supercooling to ensure solidification at room temperature. PCMs include organic PCMs, hydrated salt PCMs and alloy PCMs. Alloy PCMs are preferred for downhole thermal management systems due to their higher heat storage densities and rates than organic PCMs and lower subcooling than hydrated salt PCMs. The chosen alloy PCM has a phase change interval of 71.3 °C to 75.8 °C, a latent heat of 38400 J/kg, a specific heat capacity of 132 J/(kg·K) in the solid state and 138 J/(kg·K) in the liquid state, a density of 9660 $kg/m^3$, and a thermal conductivity of 18.42 W/(m·K).

To strengthen the heat transfer between the heat sources and the HSM, two heat transfer paths are designed in the proposed system. The first path involves direct heat conduction, including heat conduction between the heat source, the thermal interface material, the cover, the adapter, and the HSM. The other path is through a liquid cooling system. The heat sources are mounted the cold plate by TIMs, which quickly transfer the heat to the cold plate. The coolant, driven by a micropump, then transfers the heat to the HSM, where it is absorbed by the PCM.

To enhance the heat transfer in the HSM, the pipe is designed as a spiral pipe. Fig. 3(a) shows the structure of the spiral pipe, which has a spiral diameter of 50 mm, a spiral distance of 40 mm, an outer diameter

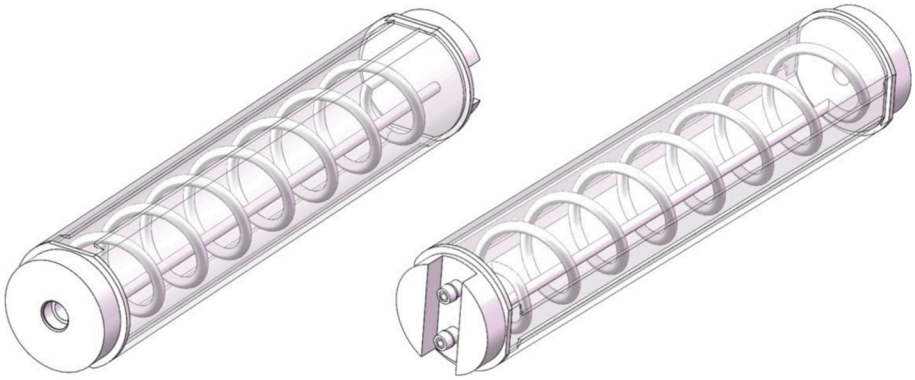

**Fig. 2.** The structure of the HSM.

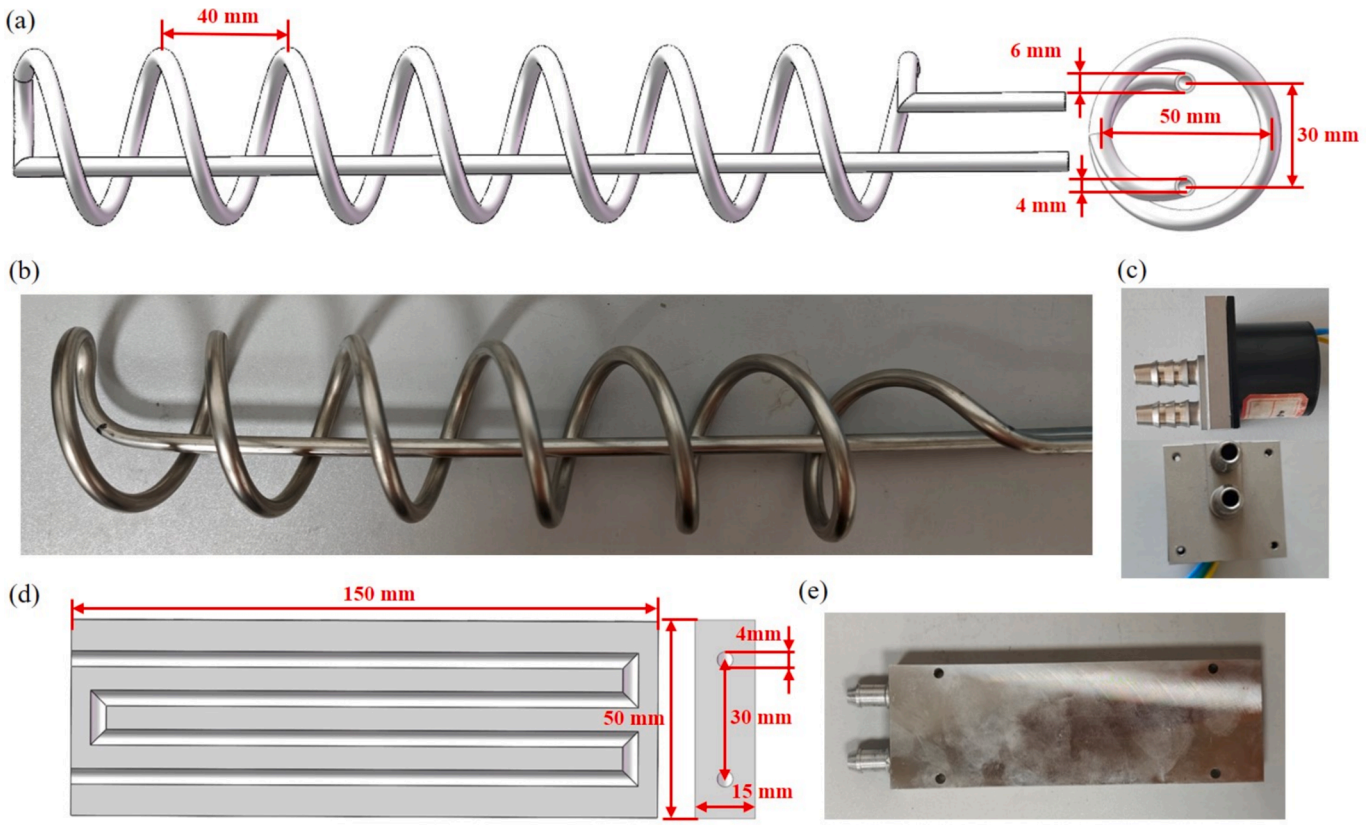


**Fig. 3.** The key components of liquid cooling system. (a) the structure of the spiral pipe; (b) the physical picture of the designed spiral pipe; (c) the micropumps used to drive the coolant; (d) the structure of the cold plate; (e) the physical picture of the cold plate.

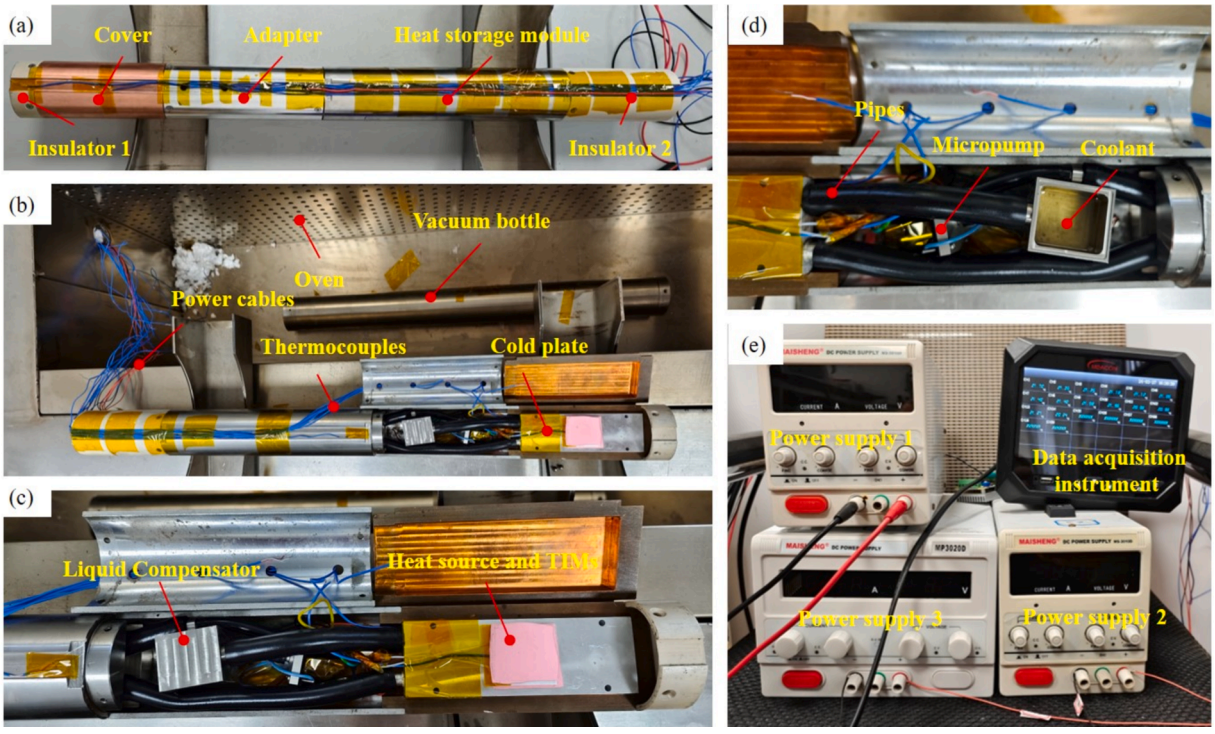


**Fig. 4.** Experimental rig. (a) The physical picture of the entire skeleton of the proposed system; (b)–(d) the physical picture outside and inside the skeleton; (e) the power supplies and data acquisition.

**Table 2**
Arrangement of temperature measurement points.

| Number | Position | Number | Position |
|---|---|---|---|
| 1 | Insulator 1 | 6 | HSM-2 |
| 2 | Cover | 7 | HSM-3 |
| 3 | Heat source | 8 | Insulator 2 |
| 4 | Adapter | 9 | Environment |
| 5 | HSM-1 | 10 | Micropump |

of 6 mm and an inner diameter of 4 mm, with the distance between the inlet and outlet of 30 mm. Fig. 3(b) shows the physical picture of the designed spiral pipe. Fig. 3(c) displays the micropumps used to drive the coolant, with dimensions of 34 mm in length, 34 mm in width, and 30.5 mm in height, provided by thermal packaging laboratory of Huazhong University of Science and Technology [45,46]. Fig. 3(d) shows the structure of the cold plate, which features an S-shaped internal flow path to maximize the heat transfer area. The cold plate measures 150 mm in length, 50 mm in width, and 15 mm in height, with a 30 mm distance between the inlet and outlet and a diameter of 4 mm. Fig. 3(e) shows the physical picture of the cold plate. Due to the high operating temperature, thermal oil is used as the coolant, with a viscosity of 100 mPa·s. It has a flash point of 300 °C and good insulating properties.

### 2.2. Experimental setup

An experimental test was conducted to test the thermal performance of the proposed thermal management system. Fig. 4(a) shows the physical picture of the entire skeleton of the proposed system, which are composed of the insulator 1, cover, adapter, HSM and insulator 2. The entire length of the skeleton was 848 mm, with the diameter of 83 mm. Fig. 4(b)-(d) show the physical picture outside and inside the skeleton. The metal vacuum bottle was used to contain the entire skeleton and insulate the heat transfer from the external high-temperature environments, as shown in Fig. 4(b). The two heat sources, consisted of the ceramic heating elements (40 mm × 40 mm × 2 mm, adjustable heating power, provided by Beijing Youpu Science and Technology Centre), were both attached in the cold plate and covers through TIMs (1 $W{\cdot}m^{-1}{\cdot}K^{-1}$, provided by Beijing Youpu Science and Technology Centre), as shown in Fig. 4 (b) and (c). The thermocouples (K-Type, 2 × 0.3 mm, accuracy 0.4 %, provided by) were fixed in several positions for temperature measurement, as shown in Table 2. The data acquisition instrument (Accuracy 0.2 % ±1 °C, MIK-6000F, provided by Hangzhou Meacon Automation Technology Company) was used for acquiring and processing thermocouple signals, as shown in Fig. (e).

The liquid cooling system was driven by the hydraulically suspended micropump (customized and provided by thermal packaging laboratory of Huazhong University of Science and Technology) with high reliability, as shown in Fig. 4(d). The coolant in the liquid compensator supplemented the fluid and promoted liquid cooling circulation. High-temperature-resistant silicone tubing connected the cold plate, micropump, liquid compensator, and HSM. In the experiments, the heating power of the micropump was approximately 4.5 W, and the flow rate of the liquid cooling circulation was about 0.2 m/s. The flow in the liquid cooling system was determined to be laminar, as calculated using the following equation.

$$Re = \frac{\rho_l u d}{\mu} \tag{1}$$

where, $Re$ is the Reynolds number, $\rho_l$ is the density of the coolant, $u$ is the velocity of coolant, $\mu$ is the dynamic viscosity of coolant, $d$ is the pipe diameter.

Fig. 5 shows a schematic of the entire experimental rig. The two heat sources were powered by the two direct current power supplies, and the micropump was powered by another DC power supplies. The entire prototype, including the vacuum bottle and the skeleton with thermocouples and heat sources, was placed in an oven for heating. The

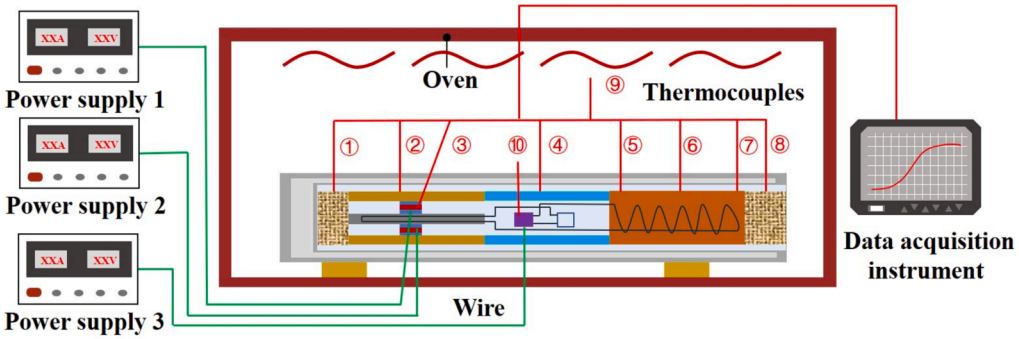


**Fig. 5.** The schematic of the entire experimental setup.

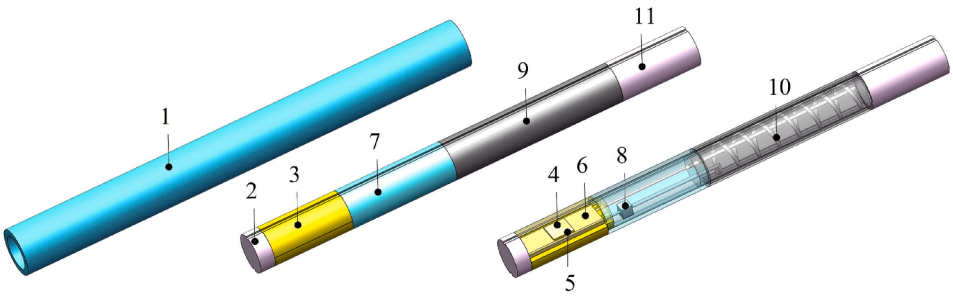


**Fig. 6.** The geometric model of the proposed TMS.

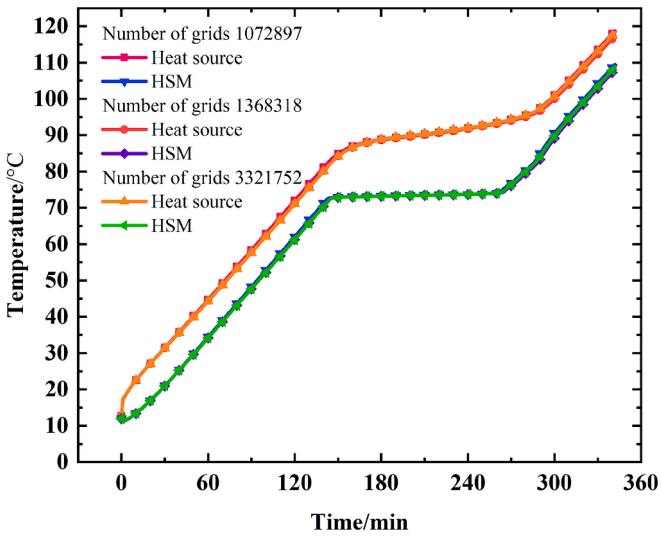


**Fig. 7.** Grid-independent validation with different number of grids.

temperature of the oven was set to 205 °C, and the stopping condition of the experiment was set to reach 125 °C for the heat sources. Experimental tests were conducted with different heat sources heating power of 20 W, 30 W and 40 W, respectively.

The uncertainty analysis of temperature measurements was performed to determine the accuracy of the results obtained in the experiments. The uncertainty in temperature measurements came from two parts: the temperature uncertainty of the thermocouples and the data acquisition instrument. Thermocouples had a temperature measurement accuracy of ±0.4 %, which means a maximum measurement error of ±0.5 °C when the temperature reached 125 °C. The measurement uncertainty of the data acquisition instrument was 0.2 % of reading ±1 °C. The maximum measure error of the data acquisition instrument was ±1.25 °C at a measurement temperature of 125 °C. The total temperature measurement uncertainty can be expressed as:

$$u(T) = \sqrt{m^2 + n^2} \tag{2}$$

where, $u(T)$ is the Uncertainty in temperature measurement, $m$ and $n$ are the Uncertainty in temperature measurement by thermocouple and data acquisition instrument, respectively.

Based on Eq. (2), the temperature reading uncertainty obtained in experiments was estimated to be ±1.34 °C when the measurement temperature was 125 °C.

## 3. Numerical model

### 3.1. Geometric model

To furtherly describe the heat transfer process in the system, a numerical heat transfer model was constructed for the proposed TMS. Fig. 6 shows the geometric model of the proposed TMS, which is the almost same to the prototype used for the experiments. The difference is that there is no fluid compensator in the simulated model, and the pipes inside the adapter is simplified.

### 3.2. Numerical heat transfer model

Due to the complexity of the system, a few assumptions were made for quick calculations according to the previous studies.

(1) The contact thermal resistance during heat transfer process was neglected [26].

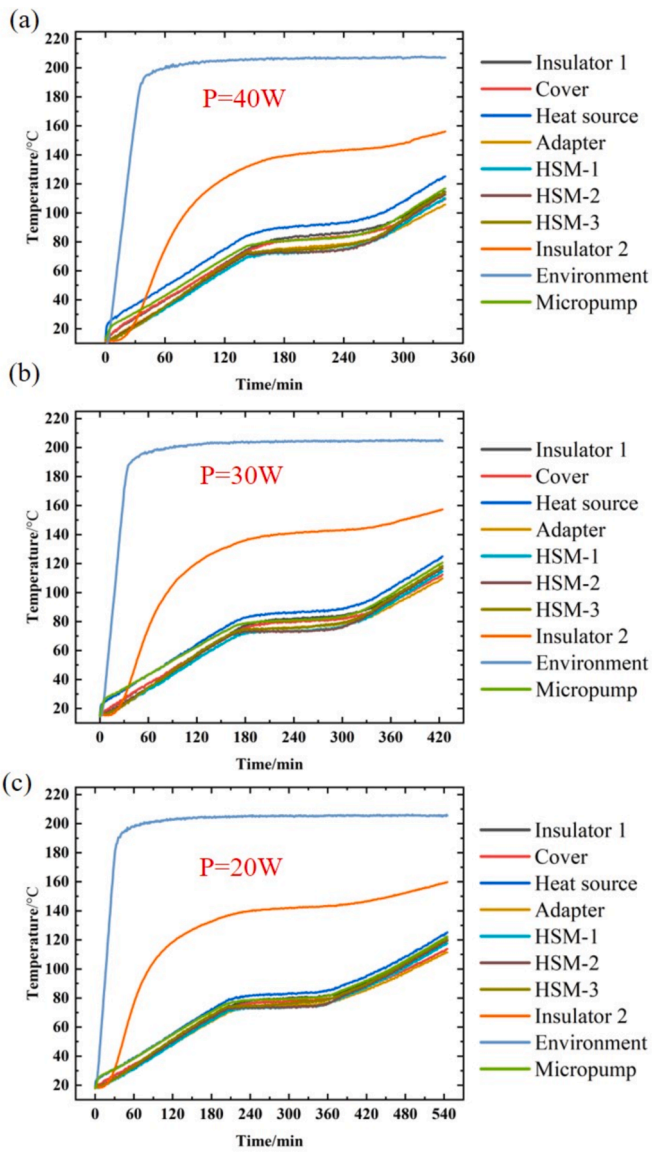


**Fig. 8.** Temperature rises curve of the proposed system at different heating powers. (a) P = 40 W; (b) P = 30 W; (c) P = 20 W.

(2) The heat sources were considered to be a body heat source that generates heat uniformly [27].
(3) Natural convection and thermal radiation inside the vacuum flask were ignored [24].
(4) The Heat transfer in the vacuum layer of the vacuum bottle was equivalent to the solid thermal conduction with a very low thermal conductivity [25].

After simplification, the heat transfer processes are divided into four parts: solid heat transfer, forced convection heat transfer through liquid cooling, phase change heat storage process, and convection heat transfer from the high-temperature mud to the vacuum flask.

The heat transfer in the solid components including the vacuum bottle, insulators, covers, cold plate, micropump, HSM and heat sources can be expressed as [47]:

$$\rho_s c_s \frac{\partial T}{\partial t} = \nabla \cdot (\lambda_s \nabla T) + q_h + q_m \tag{3}$$

Where $\rho_s$, $c_s$, $\lambda_s$, $T$ and $t$ are the density, specific heat, thermal conductivity, temperature of solid components and operation time,

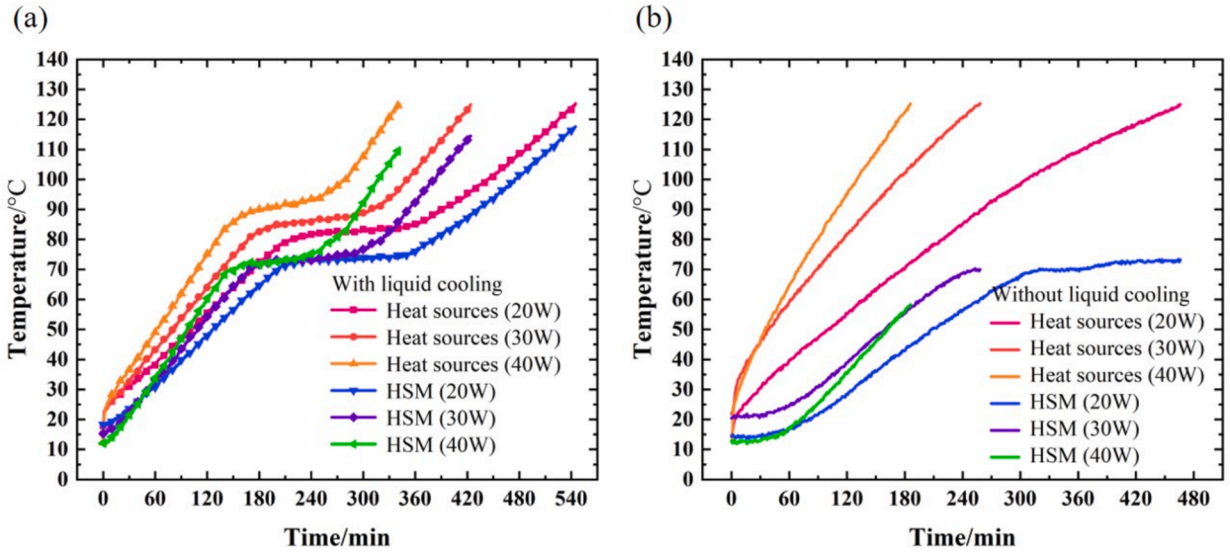


**Fig. 9.** The temperature rises curves of the heat source and HSM at various heating powers, (a) with a liquid cooling system, (b) without a liquid cooling system.

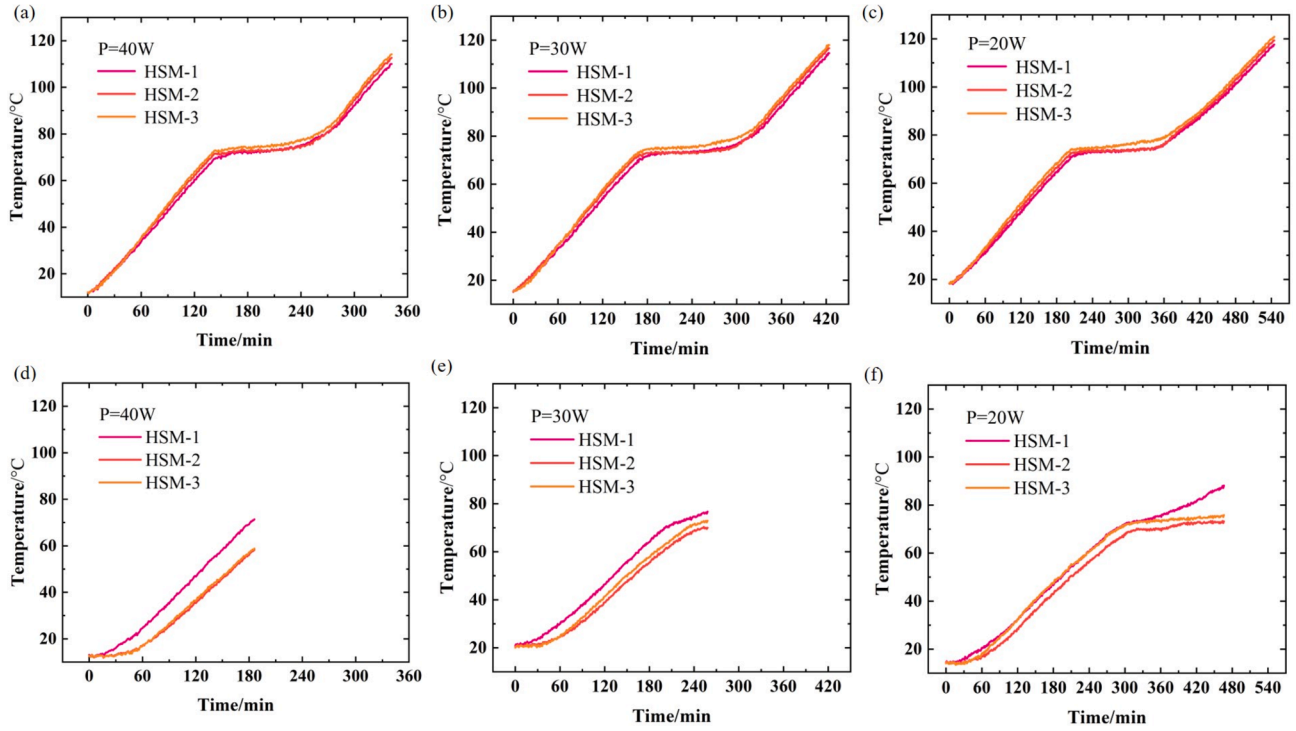


**Fig. 10.** The temperature distribution across the HSM in proposed system under different heating powers: with liquid cooling (a) P = 40 W; (b) P = 30 W; (c) P = 20 W; without liquid cooling (d) P = 40 W; (e) P = 30 W; (f) P = 20 W.

respectively. $q_h$ and $q_m$ are the heating power per unit volume of heat sources and micropump, respectively.

The forced convection heat transfer of the coolant in the liquid cooling system was calculated by coupling the continuity equation, conservation of momentum equation, and the conservation of energy equation. The continuity equation can be expressed as:

$$\frac{\partial \rho_l}{\partial t} + \nabla \cdot (\rho_l \boldsymbol{u}) = 0 \tag{4}$$

The conservation of momentum equation can be expressed as:

$$\rho_l \frac{\partial \boldsymbol{u}}{\partial t} + \rho_l (\boldsymbol{u} \cdot \nabla)\boldsymbol{u} = -\nabla P + \mu \nabla^2 \boldsymbol{u} - \varphi \tag{5}$$

Where, $P$ is the pressure of the coolant, and $\varphi$ is the Reynold stress.

The conservation of energy equation for the heat transfer process can be expressed as:

$$\rho_l c_l \frac{\partial T_l}{\partial t} + \nabla \cdot (\rho_l c_l \boldsymbol{u} T_l) = \nabla \cdot (\lambda_l \nabla T_l) \tag{6}$$

Where $\rho_l$, $c_l$, $\lambda_l$ and $T_l$ are the density, specific heat, thermal conductivity, temperature of the coolant, respectively.

The inlet and the outlet of the liquid cooling cycle was regarded as the inlet of the liquid compensator and the outlet of the micropump, respectively. The inlet of the liquid cooling system was the velocity boundary condition generated by the micropump, which was 0.2 m/s.

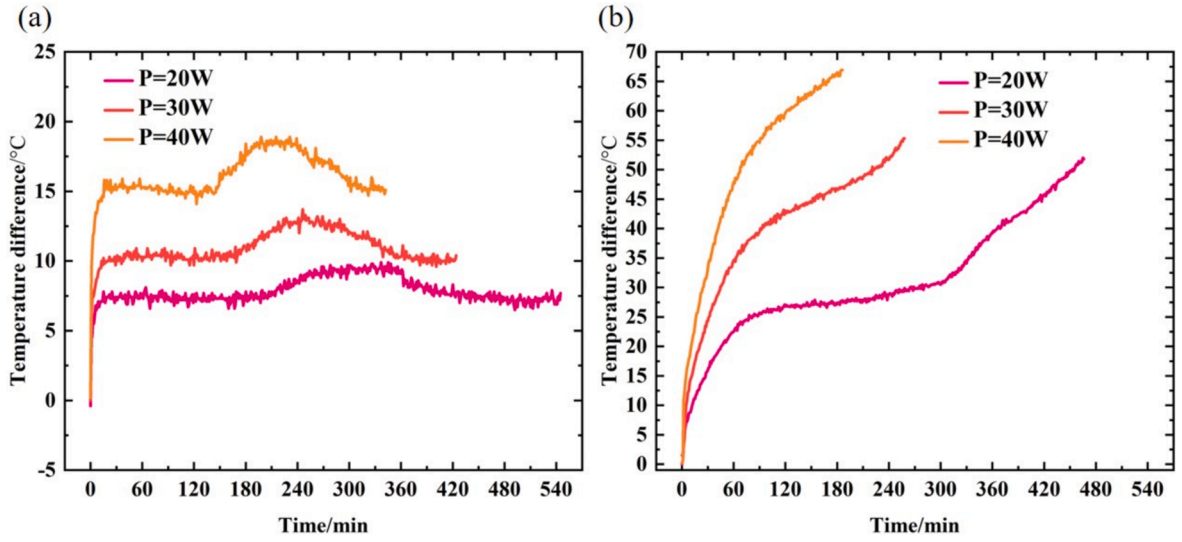


**Fig. 11.** The temperature difference between the heat source and the HSM over time at different heating powers (a) with liquid cooling, (b) without liquid cooling.

The outlet was the pressure boundary condition of the fluid flowing back to the liquid compensator. To ensure temperature continuity, the temperature of the liquid inlet and outlet are kept the same at every moment, which can be expressed as:

$$T_{in} = T_{out} \tag{7}$$

Where, $T_{in}$ and $T_{out}$ are the temperature of the liquid inlet and outlet, respectively.

For the phase change heat storage process, it is calculated by the equivalent heat capacity method [48], which can be expressed as:

$$c_{eff} = \begin{cases} c_{PCM-s} & (T < T_{\text{onset}}) \\ \frac{1}{\rho}[(1-\theta)\cdot\rho_{PCM-s}\cdot c_{PCM-s} + \theta\cdot\rho_{PCM-l}\cdot c_{PCM-l}] + \frac{L_{\text{m}}}{T_{end} - T_{onset}} & (T_{onset} \leqslant T \leqslant T_{end}) \\ c_{PCM-l} & (T_{end} < T) \end{cases} \tag{8}$$

where, $\theta$ is a function of temperature. It can be expressed as:

$$\theta = \begin{cases} 0 & (T < T_{onset}) \\ \frac{V_{PCM-l}}{V_{PCM-l} + V_{PCM-s}} & (T_{\text{onset}} \leqslant T \leqslant T_{end}) \\ 1 & (T_{end} < T) \end{cases} \tag{9}$$

The equivalent density can be expressed as:

$$\rho_{PCM} = (1-\theta)\cdot\rho_{PCM-s} + \theta\cdot\rho_{PCM-l} \tag{10}$$

The equivalent thermal conductivity can be expressed as:

$$\lambda_{PCM} = (1-\theta)\cdot\lambda_{PCM-s} + \theta\cdot\lambda_{PCM-l} \tag{11}$$

Where, $V_{PCM\text{-}s}$, $V_{PCM\text{-}l}$ mean the volume of the solid PCM and liquid PCM, $\rho_{PCM}$, $\rho_{PCM\text{-}s}$, $\rho_{PCM\text{-}l}$ mean the density of the PCM, solid PCM and liquid PCM, $\lambda_{\text{PCM}}$, $\lambda_{PCM\text{-}S}$, $\lambda_{PCM\text{-}L}$ mean the thermal conductivity of the PCM, solid PCM and liquid PCM and $c_{eff}$, $c_{PCM\text{-}s}$, $c_{PCM\text{-}s}$ mean the heat capacity of the PCM, solid PCMs and liquid PCM. $T_{onset}$ and $T_{end}$ mean phase change onset temperature and phase change end temperature of PCM, respectively. $L_m$ means the latent heat of PCM.

For the convection heat transfer from the high-temperature mud to the vacuum bottle, the average convective heat exchange coefficient can be expressed as [26]:

$$h_L = \frac{1}{L}\int_0^L h(x) = \frac{3\lambda_{\text{mud}}}{4}\left[\frac{U}{45(r_h - r_t)^2 aL}\right]^{\frac{1}{3}}\left[(11r_h - 5r_t)^{\frac{1}{3}} + \left(\frac{29r_h - 5r_t}{16}\right)^{\frac{1}{3}}\right] \tag{12}$$

Where, $h_L$ is the average convective heat exchange coefficient, $\lambda_{\text{mud}}$ is the thermal conductivity of the mud, $r_h$ is the radius of the wellbore wall, $r_t$ is the radius of the logging tool, $U$ is the velocity of the logging tool movement, $L$ is the length of the logging tool and $a$ is thermal diffusivity of the mud.

The heat exchange between the high-temperature mud and the vacuum bottle can be expressed as:

$$q_{out} = h_L(T_{mud} - T_{bottle}) \tag{13}$$

Where, $T_{mud}$ and $T_{bottle}$ are the temperature of the mud and the vacuum bottle, respectively.

### 3.3. Simulation setup and grid-independent validation

Some details of the simulation are elaborated in this section. COMSOL Multiphysics was employed to simulate the thermal performance of the proposed system. The material and the thermal properties of the proposed system was set according to Table 1. The initial temperature and inlet velocity were kept consistent with the experimental conditions. The outlet and inlet of the liquid cooling system were set as the pressure outlet boundary condition and the velocity condition, respectively. Convective heat transfer conditions were applied to the outer wall surface of the vacuum bottle. The unstructured tetrahedral meshes were used and the fluid domain was locally encrypted. The heating

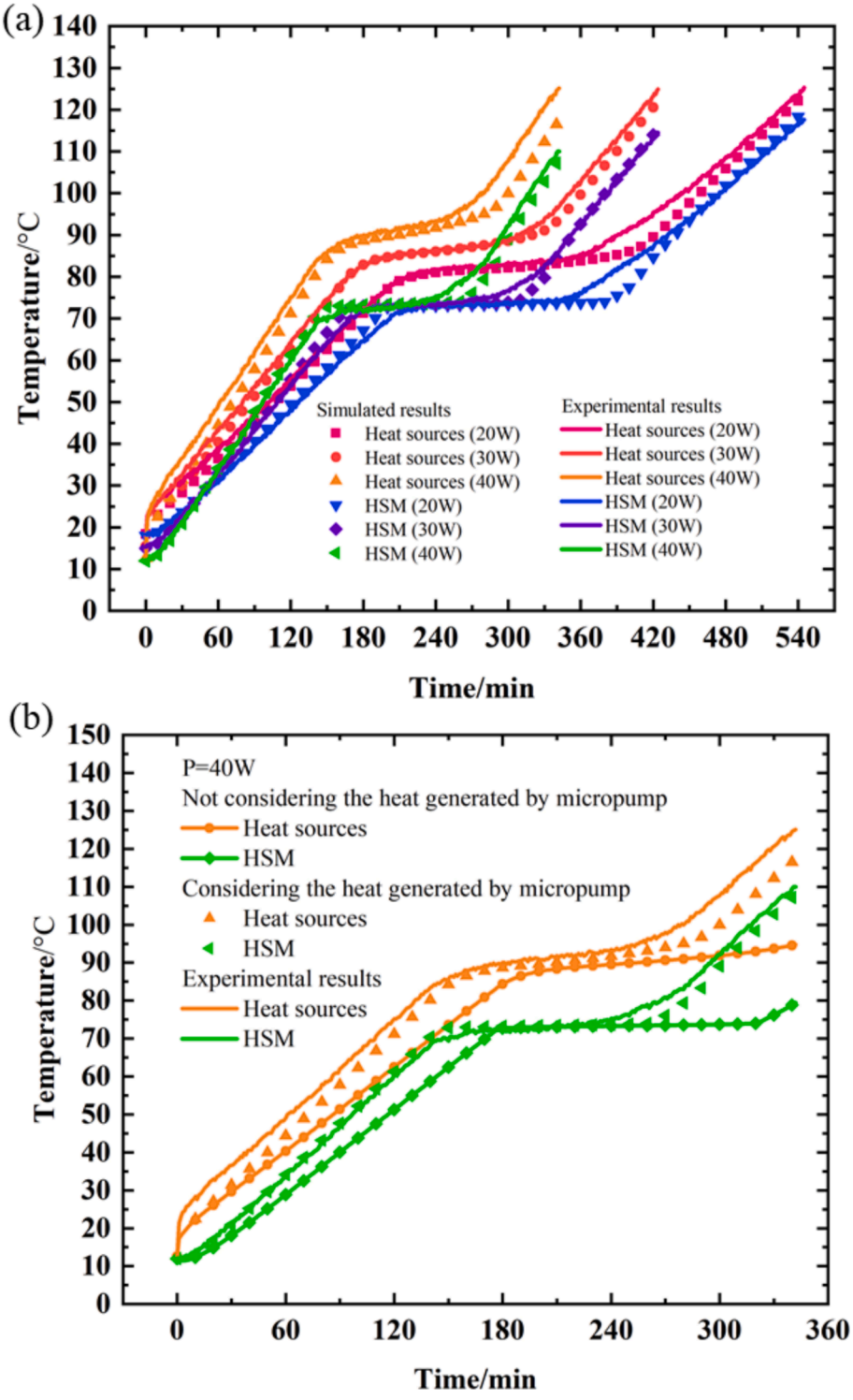


**Fig. 12.** Comparison of experimental and simulated results (a) the comparison curves of experimental and simulated temperature rise of proposed system at different heating powers; (b) simulated temperature rise under different conditions with experimental results at a heating power of 40 W.

power and calculation time in the simulations were consistent with the experiments. Convergence was judged on the basis of a relative tolerance of less than 0.0001.

Grid-independence verification was performed to obtain the accurate calculations. Fig. 7 shows the temperature curves of heat sources for different grid numbers. Considering the computational accuracy and time, grid number of 1368318 was selected for the subsequent simulations. Meanwhile, to demonstrate the accuracy of the proposed simulation method, a comparison was made with a previous simulation model that did not consider heat generation of the micropump.

## 4. Results and discussion

### 4.1. Experimental results

Fig. 8(a) shows the temperature rise curve of the proposed system

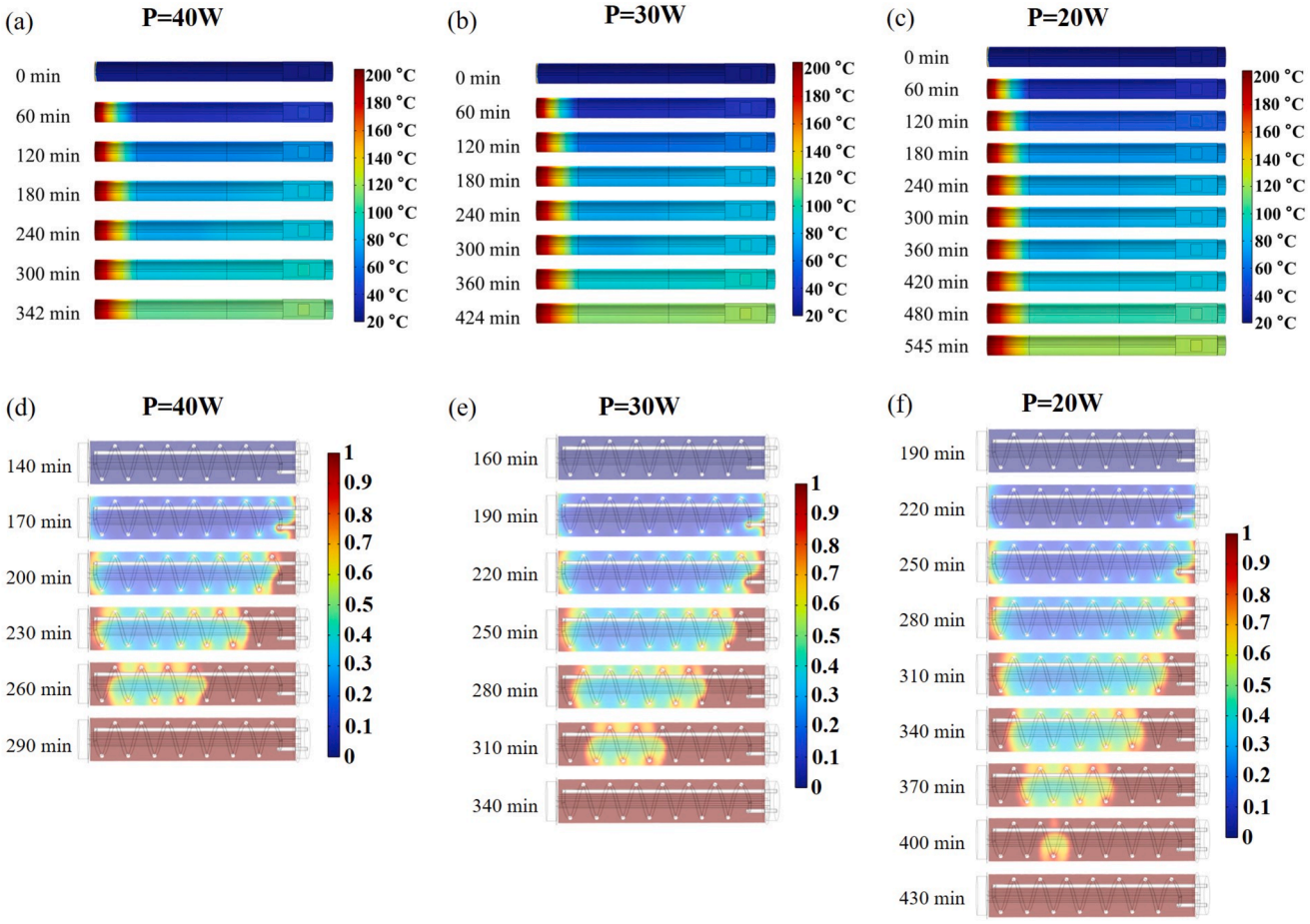


**Fig. 13.** Temperature distribution and phase transition. (a)–(c) the temperature distribution over time in the proposed system at heating powers of 40 W, 30 W, and 20 W, respectively; (b) the phase transition over time in the proposed system at heating powers of 40 W, 30 W, and 20 W, respectively.

when the heating power is 40 W. The temperature of the oven rapidly increases from room temperature to the set 205 °C within 60 min and then stabilizes. The insulator 2, located on the open side of the vacuum bottle, experiences a faster temperature rise due to more ambient greater heat intrusion. The insulator 1, on the closed side, has less ambient heat intrusion, but still shows a slightly higher temperature than the rest inside vacuum bottle except for the heat sources. The temperature rise of the heat source consists of three parts: a rapid increase as the HSM stores heat as sensible heat; a slower increase during the phase change, storing heat as latent heat; another rapid increase once the PCM is fully liquid, storing heat again as sensible heat. Overall, except for the heat source, temperature differences across the system are small due to the liquid cooling system's strong temperature uniformity and efficient heat transfer. The significant temperature difference at the heat source is due to its high heating power, which generates more heat than can be quickly transferred to the cold plate via the thermal pad, causing heat to accumulate.

Fig. 8(b) and 8(c) show the temperature rise curves of the proposed system at heating powers of 30 W and 20 W, respectively. Compared to the 40 W scenario, temperature uniformity improves significantly, and the time for the heat source temperature to reach 125 °C increases. As the power decreases, the constant temperature region of the heat source lasts longer. This improvement is due to two factors. On the one hand, at higher heating power, the heat sources generate more heat, causing the HSM to reach its capacity sooner, which shortens the phase change period. On the other hand, with increased heating power, the temperature difference between the heat source and the HSM becomes larger, reducing the heat storage capacity when the heat source temperature reaches 125 °C. At heating powers of 40 W, 30 W, and 20 W, the times for the heat source temperature to reach 125 °C are 342 min, 424 min, and 545 min, respectively.

Fig. 9(a) and (b) illustrate the temperature rise curves of the heat source and HSM with and without a liquid cooling system at various heating powers. When the liquid cooling system is off (no liquid cooling), the temperature difference between the heat source and the HSM exceeds 50 °C under different heating powers. This means that when the heat source temperature reaches 125 °C, the HSM is still undergoing phase change, indicating inefficient utilization of phase change heat storage. At heating powers of 40 W, 30 W, and 20 W, the times for the heat source temperature to reach 125 °C are 186 min, 258 min, and 466 min, respectively. In contrast, with the liquid cooling system is on (flow rate of 0.2 m/s), the temperature difference between the heat source and the HSM is significantly reduced. By the time the heat source reaches 125 °C, the temperature of the HSM has already surpassed 115 °C, indicating that the PCM inside the HSM has completed its phase change process. Therefore, the liquid cooling system exhibits much lower thermal resistance compared to traditional systems reliant solely on thermal conduction, highlighting its enhanced efficiency in thermal performance.

The experiments were stopped when the temperature of the heat source reached 125 °C. Fig. 10(a)-(c) show the temperature distribution across the HSM in proposed system under different heating powers. Temperature measurements are taken at three points: HSM-1 near the adapter, HSM-2 in the middle of the HSM, and HSM-3 close to the insulator 2. The temperature profiles show a consistent rise across the HSM-1, HSM-2, and HSM-3, with temperature differences kept within 3 °C. This uniform temperature distribution highlights the effective heat transfer capability of the liquid cooling system within the HSM. Notably,

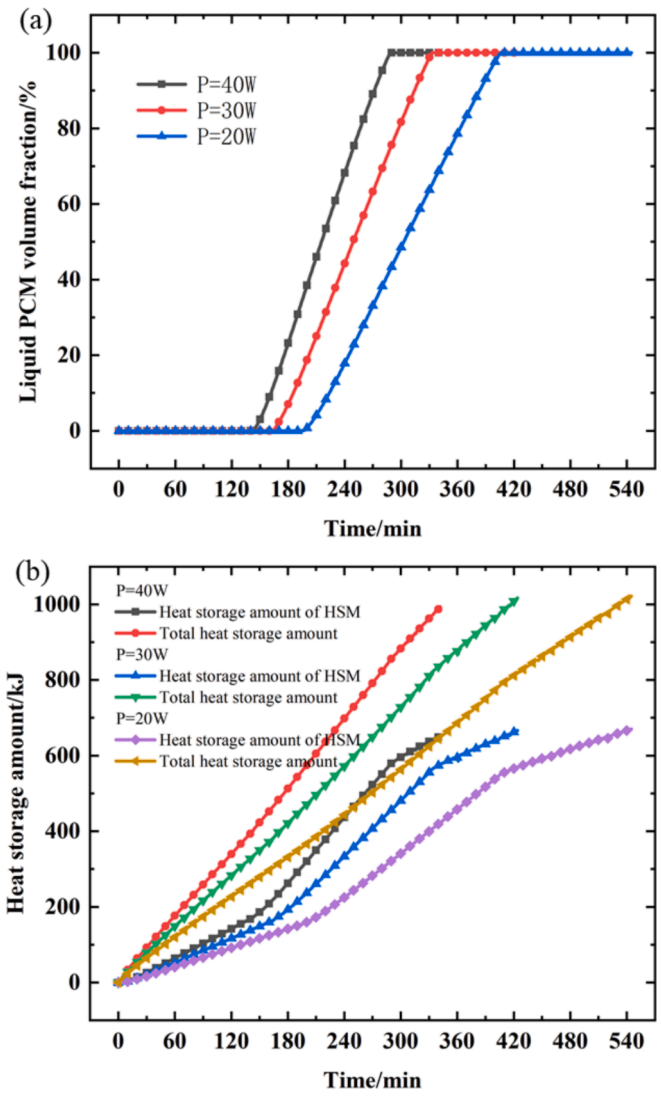


**Fig. 14.** The liquid PCM volume fraction and heat storage amount. (a) The curves of liquid PCM volume fraction over time under different heating powers; (b) the heat storage amount with time under varying heating powers.

the HSM-3, influenced more by ambient temperature due to its proximity to insulator 2, registers slightly higher temperatures compared to other regions across different heating powers. Fig. 10(d)-(f) show the temperature distribution across the HSM without liquid cooling. When the heating power is 40 W, the temperature at HSM-1 is significantly higher than the other parts, and no phase transition plateau eventually occurs. When the heating power is 20 W, the phase transition interval can be seen, but it is clearly found that the temperature at HSM-1 is higher in the phase transition interval, indicating that the temperature distribution is not uniform. Overall, due to the excellent temperature uniformity of the liquid cooling system, the HSM maintains stable temperatures, optimizing its heat storage capacity and thereby enhancing the operational duration of the system.

Fig. 11(a) depicts the temperature difference between the heat source and the HSM with liquid cooling over time at different heating powers. The temperature difference shows a pattern of initial increase, stabilization, further increase, and eventual decrease to stability. During the initial stage, as the heat source begins heating up and accumulating heat internally, its temperature rises rapidly while the HSM's temperature increases more slowly, leading to a rapid increase in the temperature difference. In the second stage, heat exchange between the heat source and the HSM stabilizes, resulting in a stabilized temperature difference. The third stage is that the heat source temperature continuing to rise, while the HSM undergoes phase change, maintaining a constant temperature and causing the temperature difference to increase further. Finally, in the fourth stage, as the HSM completes its phase transition, the temperature difference gradually decreases and stabilizes. As heating power increases from 20 W to 40 W, the maximum temperature difference between the heat source and the HSM increases from 10 °C to 18 °C. At heating powers of 20 W, 30 W, and 40 W, the final stabilized temperature differences between the heat source and the HSM are 8 °C, 10 °C, and 15 °C, respectively. As a comparison, Fig. 11(a) demonstrates the temperature difference between the heat source and the HSM without liquid cooling over time at different heating powers. The temperature differences in the final moments at different heating powers both exceed 50 °C, with a maximum of 66.9 °C.

### 4.2. Comparison of experimental and simulated results

Fig. 12(a) shows the comparison curves of experimental and simulated temperature rise of proposed system at different heating powers. The simulation model accounts for the self-heating of the heat source and the pump. The comparison shows a good agreement between the trends of the simulation and experimental results, with a maximum error of less than 6 % across all tested conditions. Notably, the experimental heat source temperatures are generally lower than those predicted by simulation. Several factors contribute to this temperature difference. First, the simulation neglects contact thermal resistance, which can affect heat transfer efficiency. This oversight leads to smaller temperature differences between the heat source and the HSM in the simulation, with the largest error observed at 40 W power. Second, Higher actual ambient heat intrusion in experiments compared to simulations affects temperature profiles. Third, Uncertainty in experimental temperature measurements introduces some discrepancies. Overall, despite these factors, the small error between simulation and experimental results validates the simulation model's capability to analyse the thermal performance of the system effectively.

Fig. 12(b) compares simulated temperature rise under different conditions with experimental results at a heating power of 40 W. The comparison includes simulations without considering the pump's self-heating and simulations that account for the pump's self-heating, while other conditions remain consistent. It is evident that simulations neglecting the pump's self-heating exhibit significant discrepancies compared to experimental results. The temperature trends and stable temperature platforms differ notably between these simulations and experiments. Conversely, when the pump's self-heating is considered in the simulation, the results closely align with experimental findings. This underscores the importance of including the pump's heat generation in simulations for accurately predicting the thermal performance of the proposed system. The analysis of the system's thermal performance should utilize simulation models that appropriately account for the pump's self-heating to ensure accurate and reliable results.

### 4.3. Thermal performance of the proposed system

Fig. 13(a)-(c) depict the temperature distribution over time in the proposed system at heating powers of 40 W, 30 W, and 20 W, respectively. The highest temperatures are observed at insulator 2, positioned on the opening side of the thermos bottle, where it is most influenced by the high-temperature environment. However, due to effective thermal insulation of insulator 2, a noticeable temperature gradient exists, with temperatures decreasing closer to the HSM. Overall, except for insulator 2, temperature distribution is relatively uniform across different heating power conditions. Temperatures steadily increase over time in other areas. At 40 W heating power, temperatures at 180 min and 240 min remain nearly unchanged; at 30 W heating power, temperatures at 180 min, 240 min, and 300 min show little change; and at 20 W heating power, temperatures at 180 min, 240 min, 300 min, 360 min, and 420

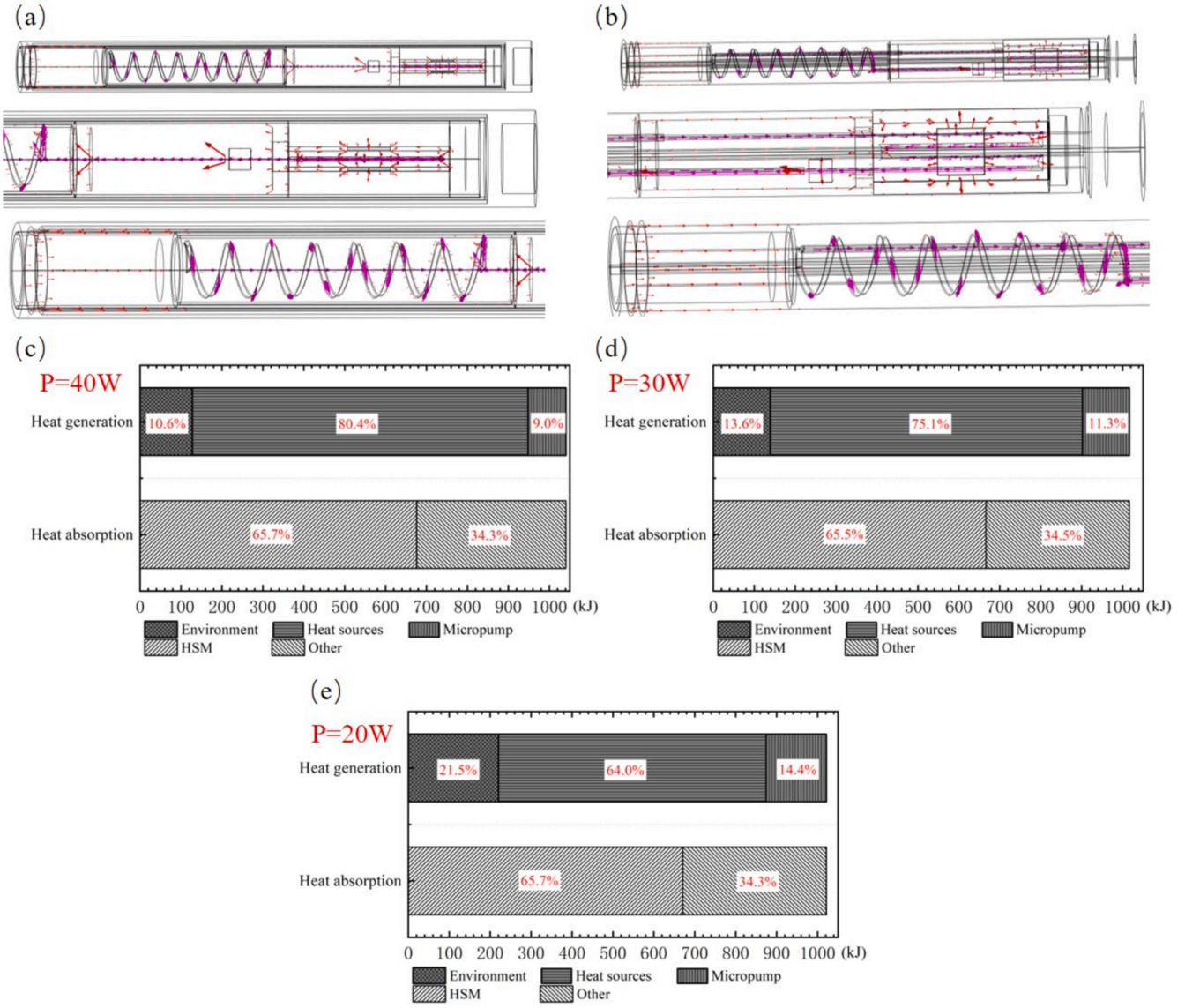


**Fig. 15.** Heat flow, heat generation and absorption. (a)-(b) The internal heat flow of the proposed system; (c)-(e) the percentage distribution of heat generation and absorption under different heating powers in the proposed system.

min exhibit minimal variation. This constancy is primarily due to the HSM undergoing phase transition during these periods, storing heat as latent heat and maintaining a steady temperature. This stability helps suppress temperature increases in the heat source, resulting in consistent temperature distribution over time.

Fig. 13(d)-(f) illustrate the phase transition over time in the proposed system at heating powers of 40 W, 30 W, and 20 W, respectively. In these figures, "0″ represents the solid state, "1″ indicates the liquid state, and "0-1″ marks the transition region where both solid and liquid states coexist. The PCM within the HSM transitions from solid to liquid, moving from both ends towards the middle. This movement is influenced by heat intrusion from the high-temperature environment and heat generated by the heat sources. Observations show that the PCM largely absorbs heat generated by the heat sources, leading to phase change progression. By the final stage, PCM has completed its transition from solid to liquid. Notably, phase change initiation typically begins near the spiral pipe attachment and gradually extends outward, starting near the heat source and insulator 2. This highlights the proposed system's efficacy in enhancing heat transfer within the HSM, facilitating rapid heat transfer from the spiral pipes to the PCM for storage.

Fig. 14(a) displays the curves of liquid PCM volume fraction over time under different heating powers. As heating power increases, the phase transition rate of the PCM accelerates, resulting in shorter phase transition intervals and earlier phase transition initiation. Specifically, at heating powers of 40 W, 30 W, and 20 W, the phase transition intervals for the HSM are 194–406 min, 162–333 min, and 140–289 min, respectively. By the final moments depicted, all PCMs within the HSM have completed their transition from solid to liquid. Fig. 14(b) illustrates the heat storage amount with time under varying heating powers. Both the total heat storage amount and the heat storage amount of the HSM exhibit minor increases with higher heating powers. Notably, the heat storage rate experiences a significant boost during the phase transition of the HSM. At heating powers of 40 W, 30 W, and 20 W, the heat storage amount of the HSM reaches 652.7 kJ, 666.3 kJ, and 670.5 kJ, respectively, while the total heat storage amounts to 993.7 kJ, 1016.8 kJ, and 1021.4 kJ, respectively. These values underscore the system's ability to efficiently store and utilize heat during operation.

Fig. 15(a)-(b) illustrate the internal heat flow of the proposed system. In the diagram, red arrows denote heat flow via heat conduction, while magenta arrows represent convective heat transfer. The diagram shows that a portion of the heat generated by the heat source is rapidly transferred to the HSM through the liquid cooling system. Within the

HSM, a spiral pipeline facilitates heat diffusion outward. Additionally, some heat is transferred via the "thermal bridge effect," bypassing the thermal insulators and transferring through the skeleton to be absorbed by the HSM. It is evident that heat transfer through the liquid cooling system outweighs heat transfer through the skeleton. This highlights the critical role of the liquid cooling system in the proposed system.

Fig. 15(c)-(e) present the percentage distribution of heat generation and absorption under different heating powers in the proposed system. Heat generation primarily comprises environmental heat intrusion, heat from the heat source and micropump. Conversely, heat absorption includes the HSM and other components. Regarding heat generation, as heating power increases, the operational duration of the heat source decreases, leading to reduced ambient heat intrusion and pump heat. Consequently, the proportion of heat generated by the heat source increases. At heating powers of 40 W, 30 W, and 20 W, the heat generated by the heat source accounts for 80.4 %, 75.1 %, and 64.0 % of the total heat, respectively, while environmental heat intrusion constitutes 10.6 %, 13.6 %, and 21.5 % correspondingly. This illustrates that the heat generated by the heat sources forms a significant portion of the total heat. In terms of heat absorption, the proportion of heat stored in the HSM relative to the total heat storage remains nearly constant. This stability arises from the thermal structure where heat stored in the HSM and its components reaches a certain temperature, maintaining consistent heat storage levels. At heating powers of 40 W, 30 W, and 20 W, the heat storage capacity of the HSM accounts for 65.7 %, 65.5 %, and 65.7 % of the total heat storage capacity, respectively, highlighting its pivotal role in heat storage. Overall, the proposed system primarily generates heat from the heat source and predominantly stores heat within the HSM, demonstrating its effective thermal management capability.

## 5. Conclusions

A high-temperature HTMS integrating liquid cooling and PCM is proposed to extend the effective operation duration of downhole electronics. In this system, the self-generated heat of the electronics was transferred to the HSM efficiently through liquid cooling, which drastically reduces the thermal resistance between the downhole electronics and the HSM, thereby extending the operational duration of the electronics. The conclusion are as follows.

1) The experimental setup of the proposed HTMS was established to evaluated the thermal management performance. The experimental results show that the temperature differences between the electronics and the HSM remained below 15 °C for heating powers of 20 W, 30 W and 40 W.
2) Compared to the system without liquid cooling, the temperature difference between the heat source and the heat storage module (HSM) was reduced by up to 51.9 °C, and the working time was increased by up to 166 mins. This demonstrates the excellent thermal performance of the introduced liquid cooling system.
3) The numerical model of the proposed HTMS was constructed, and the accuracy was verified by experimental results, with maximum deviation less than 6 %. Through this model, the temperature distribution, phase change characteristics, heat flow dynamics, and the percentage of heat generation and absorption were analysed. The heat storage of the HSM accounts for more than half of the total heat storage, and the environmental heat intrusion is only 21.5 % at the highest.

Overall, the proposed system can effectively reduce the temperature difference between the heat source and HSM, and improve the working time of the heat source, which has a better application prospect. However, while existing structures in this study can have good thermal management performance, superior performance can be achieved through structural and strategic optimization.

## Author contributions

**Jiale Peng:** Conceptualization, Methodology, Investigation, Data curation, Validation, Writing – original draft. **Jiacheng Li & Siqi Zhang:** Data curation, Methodology. **Guanying Xing:** Data curation, Discussion. **Jinlong Ma:** Discussion, Funding acquisition. **Bofeng Shang:** Methodology, Supervision, Writing – review & editing. **Xiaobing Luo:** Conceptualization, Supervision, Writing – review & editing, Funding acquisition.

## Declaration of competing interest

The authors declare that they have no known competing financial interests or personal relationships that could have appeared to influence the work reported in this paper.

## Acknowledgement

This research was supported by National Key Research and Development Program of China (2022YFC2204400) and the Open Fund Science and Technology on Thermal Energy and Power Laboratory (No. TPL2022B02).

## Data availability

Data will be made available on request.

## References

[1] Z. Wang, Z. Fan, X. Chen, et al., Global oil and gas development in 2022: Situation, trends and enlightenment, Pet. Explor. Dev. 50 (2023) 1167–1186.
[2] H. Oh, S. Akar, K. Beckers, et al., Techno-economic feasibility of geothermal energy production using inactive oil and gas wells for district heating and cooling systems in Tuttle, Oklahoma, Energy Convers. Manage. 308 (2024) 118390.
[3] M. Macenić, T. Kurevija, I. Medved, Novel geothermal gradient map of the Croatian part of the Pannonian Basin System based on data interpretation from 154 deep exploration wells, Renew. Sustain. Energy Rev. 132 (2020) 110069.
[4] Z. Cao, A. Ma, Q. Xu, et al., Geochemical characteristics and exploration significance of ultra-deep Sinian oil and gas from Well Tashen 5, Tarim Basin, NW China, Energy Geosci. 5 (1) (2024) 100217.
[5] L. Mao, X. Chen, Y. Gao, et al., Vibration characteristics and safety analysis of production string in high temperature, high pressure gas wells, Geoenergy Sci. Eng. (2024) 212959.
[6] S. Wang, X. Chen, M. He, et al., Coupled modeling circulating multi-layer wellbore temperature and stress field during deepwater high-temperature and high-pressure gas well testing, Therm. Sci. Eng. Prog. 47 (2024) 102356.
[7] F. Wei, W. Lan, C. Deng, et al., A transient thermal model for forecasting the real-time temperature of downhole electronics, Int. J. Therm. Sci. 200 (2024) 108946.
[8] F. Li, Y. Liu, X. Ma, et al., Design of 150° C DC-DC converter based on flyback topology for downhole drilling equipment, IEEE Access 11 (2023) 111126–111132.
[9] M.S. Khaled, N. Wang, P. Ashok, et al., Strategies for prevention of downhole tool failure caused by high bottomhole temperature in geothermal and HPHT oil and Gas Wells, SPE/IADC Drilling Conference and Exhibition. SPE (2023). D031S020R002.
[10] B. Shang, Y. Ma, R. Hu, et al., Passive thermal management system for downhole electronics in harsh thermal environments, Appl. Therm. Eng. 118 (2017) 593–599.
[11] Y. Ma, B. Shang, R. Hu, et al., Thermal management of downhole electronics cooling in oil & gas well logging at high temperature, in: 2016 17th International Conference on Electronic Packaging Technology (ICEPT), 2016, pp. 623–627.
[12] Y. Lv, W. Chu, Q. Wang, Thermal management systems for electronics using in deep downhole environment: A review, Int. Commun. Heat Mass Transfer 139 (2022) 106450.
[13] J. Zhang, W. Lan, C. Deng, et al., Thermal optimization of high-temperature downhole electronic devices, IEEE Trans. Compon. Packag. Manuf. Technol. 11 (11) (2021) 1816–1823.
[14] M. Wei, W. Cai, M. Xu, et al., Active cooling system for downhole electronics in high-temperature environments, J. Therm. Sci. Eng. Appl. 14 (8) (2022) 081009.
[15] Q. Tao, M. Wei, H. Chen, et al., Thermal management system of vapor compression for downhole instrument, J. Therm. Sci. Eng. Appl. 15 (9) (2023).
[16] G. Xu, Z. Jing, X. Haiming, et al., Downhole circulating cooling device, J. Phys.: Conf. Ser. IOP Publish. 1894 (1) (2021) 012047.
[17] W. Gao, K. Liu, X. Dou, et al., Numerical investigation on cooling effect in the circuit cabin of active cooling system of measurement-while-drilling instrument based on split-Stirling refrigerator, Case Stud. Therm. Eng. 28 (2021) 101621.

[18] S. Tang, W. Gao, K. Liu, Design and numerical study of active cooling system of measurement while drilling for high temperature based on supersonic, Case Stud. Therm. Eng. 50 (2023) 103460.
[19] S. Tang, Z. Liang, Y. Zhu, Numerical investigation on heat transfer characteristics in electronic cavity of downhole measurement-while-drilling system, J. Therm. Sci. Eng. Appl. 13 (1) (2021) 011022.
[20] S. Soprani, J.H.K. Haertel, B.S. Lazarov, et al., A design approach for integrating thermoelectric devices using topology optimization, Appl. Energy 176 (2016) 49–64.
[21] W. Gao, K. Liu, X. Dou, L. Zhang, S. Tang, Numerical investigation on heat transfer rate from the outside environment into the electronic compartment of the measurement-while-drilling tools, Heat Transfer 50 (2021) 5835–5852.
[22] R. Weerasinghe, T. Hughes, Analysis of thermal performance of geophonic downhole measuring tools; a numerical and experimental investigation, Appl. Therm. Eng. 137 (2018) 504–512.
[23] Z. Wan, F. Wei, J. Peng, et al., Application of physical model-based machine learning to the temperature prediction of electronic device in oil-gas exploration logging, Energy 282 (2023) 128973.
[24] J. Peng, Z. Tian, C. Deng, et al., Durable and reliable thermal management system with superior temperature uniformity for sidewall coring tool in extreme thermal environments, Therm. Sci. Eng. Prog. 51 (2024) 102635.
[25] J. Peng, Y. Wang, S. Ding, et al., Rapid detection of the vacuum failure of logging tools based on the variation in equivalent thermal conductivity, Int. J. Therm. Sci. 188 (2023) 108245.
[26] J. Peng, W. Lan, F. Wei, et al., A numerical model coupling multiple heat transfer modes to develop a passive thermal management system for logging tool, Appl. Therm. Eng. 223 (2023) 120011.
[27] J. Peng, W. Lan, C. Deng, et al., An improved numerical model based on the equivalent thermal conductivity method for downhole thermal management systems, Int. Commun. Heat Mass Transfer 152 (2024) 107317.
[28] C. Deng, F. Wei, W. Lan, et al., Experimental and numerical investigation of low melting point alloy for downhole electronics at high temperature, IEEE Int. Power Elect Appl. Con. Expo. (PEAC) IEEE 2022 (2022) 49–54.
[29] J. He, Q. Wang, J. Wu, et al., Hybrid thermal management strategy with PCM and insulation materials for pulsed-power source controller in extreme oil-well thermal environment, Appl. Therm. Eng. 214 (2022) 118864.
[30] S. Ma, S. Zhang, Y. Zhao, et al., Thermal insulation and shock shielding effects of PCM capsules using for downhole pulsed power source device, Int. J. Heat Mass Transf. 230 (2024) 125774.
[31] W. Lan, J. Zhang, J. Peng, et al., Distributed thermal management system for downhole electronics at high temperature, Appl. Therm. Eng. 180 (2020) 115853.
[32] J. Peng, W. Lan, Y. Wang, et al., Thermal management of the high-power electronics in high temperature downhole environment, in: 2020 IEEE 22nd Electronics Packaging Technology Conference (EPTC), 2020, pp. 369–375.
[33] F. Wei, C. Deng, J. Peng, et al., Thermal optimization of a logging tool used in high temperature downhole environment, in: 2022 IEEE International Power Electronics and Application Conference and Exposition (PEAC), IEEE, 2022, pp. 72–77.
[34] H. Zhou, X. Guo, L. Xu, et al., Thermal performance of a hybrid thermal management system that couples PCM/copper foam composite with air-jet and liquid cooling, J. Storage Mater. 74 (2023) 109408.
[35] X. Xu, Y. Su, J. Kong, X. Chen, X. Wang, H. Zhang, et al., Performance analysis of thermal management systems for prismatic battery module with modularized liquid-cooling plate and PCM-negative Poisson's ratio structural laminboard, Energy 286 (2024) 129620.
[36] L. Rong, X. Bai, J. Li, R. Zhang, W. Yang, Design and optimization of a hybrid cooling configuration combining PCM and liquid cooling for Li-ion battery using data-based response surface approximation model, Appl. Therm. Eng. 245 (2024) 122844.
[37] Y. Zhao, B. Zou, J. Ding, Y. Ding, Experimental and numerical investigation of a hybrid battery thermal management system based on copper foam-paraffin composite phase change material and liquid cooling, Appl. Therm. Eng. 218 (2023) 119312.
[38] Q. Xin, T. Yang, H. Zhang, J. Yang, J. Zeng, J. Xiao, Experimental and numerical study of lithium-ion battery thermal management system using composite phase change material and liquid cooling, J. Storage Mater. 71 (2023) 108003.
[39] J. Peng, W. Lan, F. Wei, et al., Thermal management for high-power downhole electronics using liquid cooling and PCM under high temperature environment, in: IEEE 24th Electronics Packaging Technology Conference (EPTC), IEEE, 2022, pp. 935–940.
[40] J.C. Jakaboski, Innovative thermal management of electronics used in oil well logging, Georgia Institute of Technology, 2004.
[41] S. Ma, S. Zhang, J. Wu, et al., Experimental study on active thermal protection for electronic devices used in deep− downhole− environment exploration, Energies 16 (3) (2023) 1231.
[42] J. Peng, C. Deng, F. Wei, et al., A hybrid thermal management system combining liquid cooling and phase change material for downhole electronics, J. Storage Mater. 72 (2023) 108610.
[43] B. Shang, G. Yang, B. Zhang, Phase change nanocapsules incorporated with nanodiamonds for efficient photothermal energy conversion and storage, Appl. Energy 360 (2024) 122806.
[44] C. Deng, X. Zhang, J. Peng, et al., In51Bi32. 5Sn16. 5@ SiO2 microcapsules-based composite phase change materials with high thermal conductivity and heat storage density for electronics thermal management, J. Energy Storage 86 (2024).
[45] G. Xing, S. Xue, T. Hong, et al., A novel hydrodynamic suspension micropump using centrifugal pressurization and the wedge effect, Sci. China Technol. Sci. 66 (7) (2023) 2047–2058.
[46] G. Xing, S. Xue, J. Han, et al., Turbulent lubrication model for journal-axial coupled hydrodynamic bearings without grooves, Tribol. Int. 190 (2023) 109036.
[47] J.P. Holman, Heat transfer (10th Edition), McGraw Hill Education, New York, 2009.
[48] X. Ying, N. Xin, C. Qinglin, et al., Phase-change heat transfer analysis of shutdown overhead pipeline, Case Stud. Therm. Eng. 13 (2019) 100399.